International Journal of Mechanical Sciences 242 (2023) 108016

Contents lists available at ScienceDirect

International Journal of Mechanical Sciences

journal homepage: www.elsevier.com/locate/ijmecsci

Etching metasurfaces on bluff bodies for vortex-induced vibration energy harvesting

Junlei Wang [a], Ye Zhang [a], Ming Liu [a], Guobiao Hu [b,c,*]

[a] *School of Mechanical and Power Engineering, Zhengzhou University, China*
[b] *Internet of Things Thrust, The Hong Kong University of Science and Technology (Guangzhou), China*
[c] *School of Civil and Environmental Engineering, Nanyang Technological University, Singapore*

ARTICLE INFO

Keywords:
Vortex-induced vibration
Energy harvesting
Metasurface
Aerodynamics
Piezoelectric

ABSTRACT

Bluff bodies play crucial roles in affecting the functionality of wind energy harvesting systems. Inspired by the versatility and wide application of metasurfaces in many fields, we propose to etch several metasurface patterns on a cylinder bluff body and investigate their effects on vortex-induced vibration (VIV). A general lumped parameter model is developed for VIV piezoelectric energy harvesters (VIVPEHs). Three-dimensional CFD simulation models are built to obtain the lift and drag coefficients. Wind tunnel tests are conducted to experimentally study the dynamics and evaluate the voltage output. The theoretical results matched well with the experimental ones. It is unveiled that etching the concave metasurface patterns on the bluff bodies has a significant influence on the dynamic behavior of the bluff body, thus enhancing or suppressing VIV. Beside, we demonstrate the influences of the etched metasurface patterns on the generated vortex street behind the bluff bodies through CFD simulations. It is shown that different concave metasurface patterns could significantly affect the wake pressure, thus influencing the aerodynamics. Furthermore, the effects of the electrical parameters, including the load resistance and electromechanical coupling strength, on energy harvesting performance are investigated based on the theoretical model.

1. Introduction

Bluff bodies can be widely discovered in many engineering structures and systems, such as chimneys [1], heat exchangers [2,3], heating ventilation and air condition (HVAC) systems [4], and marine risers [5]. Fluid-induced vibration (FIV) occurs due to the fluid flow interaction with bluff body structures [6–9]. FIV can greatly reduce the service life of systems by causing structural fatigue damage, thus usually treated as a disruptive phenomenon. In recent years, the power consumption of micro-electro-mechanical systems (MEMS) has been tremendously lowered with the fast development of MEMS technology. However, advancements in battery technology have been relatively sluggish. Chemical batteries are bulky, toxic, and have limited lifespans. Driven by the rapidly rising demand for implementing millions and even billions of Internet of Things (IoTs) nodes, researchers proposed to develop sustainable and environmentally friendly energy technologies [10–13]. Since fluidic flows ubiquitously exist around the world, leveraging FIV phenomena for harnessing energy from the ambient environment has attracted enormous research interest. Piezoelectric [14–17], electromagnetic [18–21], electrostatic [22–24], triboelectric [25–28], and thermoelectric [29] transductions are the several most commonly used energy conversion mechanisms. By virtue of the high-power density, low bare cost, and ease of integration, piezoelectric materials have been extensively used in designing various kinds of energy harvesting systems.

Flow-induced vibration (FIV) is a relatively wide concept that includes vortex-induced vibration (VIV) [30–33], galloping [34–37], flutter [38–40], and buffeting [41–43]. VIV is more inclined to take place at relatively low wind speeds and thus has received much attention. Lots of studies have been conducted on the topic of VIV energy harvesting from various aspects. Bishop and Hassan [44] showed that the VIV of a cylinder bluff body is a self-limiting oscillation through an experimental study and suggested the existence of “wake oscillator”. Dai et al. [45] developed a nonlinear continuous model of a piezoelectric cantilever beam equipped with a cylinder bluff body for VIV energy harvesting. Wang et al. [46] developed an equivalent circuit model (ECM) for a general VIVPEH based on the Ehsan-Scanlan model. Gu et al. [47] numerically investigated the influence of the submergence depth

---

* Corresponding author at: Internet of Things Thrust, The Hong Kong University of Science and Technology, Guangzhou, China.
E-mail address: guobiaohu@hkust-gz.edu.cn (G. Hu).

https://doi.org/10.1016/j.ijmecsci.2022.108016
Received 30 September 2022; Received in revised form 19 November 2022; Accepted 6 December 2022
Available online 7 December 2022

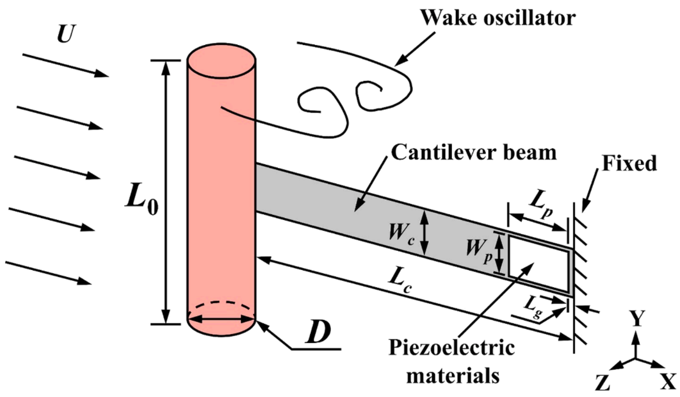

Fig. 1. Diagram of the vortex-induced vibration-based piezoelectric energy harvester (VIVPEH). The near-wake motion is described by the van der Pol equation. A small gap between the PZT patch and the clamped end is to prevent damage due to stress concentration.

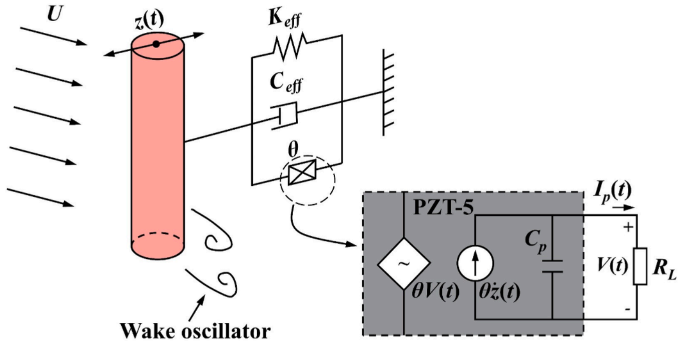

Fig. 2. A simplified SDOF model of the VIVPEH. The piezoelectric element in the electrical domain is treated as a current source.

on the energy conversion of a smooth cylinder. They noticed that the vibration amplitude and power output stopped increasing if the submergence depth exceeded 0.5 m. Zhang et al. [48] introduced the Lorentz force in VIV and found that the Lorentz force has significant influences on the displacement, lift force, and drag force.

Since bluff bodies play essential roles in affecting the functionality of wind energy harvesters, researchers attempted to change their shapes to enhance energy harvesting efficiency. Ding et al. [49] compared the performance of different bluff bodies for FIV energy harvesting and found that a trapezoid-sectioned bluff body performed best. Zhu et al. [50] studied the effect of the splitter plate on the aerodynamics of a cylinder bluff body. It was unveiled that the splitter plate installed upstream of the bluff body could suppress VIV. Ding et al. [51] added symmetrical fin-shaped rods to a cylinder bluff body for realizing energy harvesting over a broad wind speed range. Zhou et al. [52] designed an energy harvester consisting of two magnetically coupled beams attached with cylinder bluff bodies. The experimental results showed that the lock-in region of the system significantly increased, and the power output increased by 679% compared with a conventional counterpart. Wang et al. [53] developed a cylinder bluff body with Y-shaped ornaments to realize VIV-to-galloping transition and greatly widened the effective bandwidth. Ranjbar et al. [54] demonstrated the efficiency sensitivity of a wind energy harvester to the aspect ratio change of the bluff body. They found that the oscillation amplitude increased by 230% when the aspect ratio reduced from 28.8 to 5.0.

In addition to substantially changing the geometric shapes of bluff bodies, other researchers found that introducing surface treatment to the bluff bodies could also remarkably alter their aerodynamic behaviors. Gao et al. [55] investigated the aerodynamics of a circular bluff body with different surface roughness. It was noted that the displacement amplitude of the bluff body displayed an increasingly prominent jumping characteristic with the increase of the surface roughness. Huang et al. [56] conducted an experiment and suppressed the VIV of a cylinder bluff body by 64% by introducing helical grooves. Zhu et al. [57] studied the FIV of a cylinder bluff body attached with a rigid wavy splitter. The results indicated a reduction in cross-flow amplitude up to 92.44% at a particular wind speed. Jin et al. [58] added different bionic attachments on a smooth cylinder and found that different types and numbers of attachments had significant effects on energy harvesting performance. Wang et al. [59] explored the influences of different convex metasurfaces on energy harvesting performance. They found that convex metasurfaces changed the flow fields formed behind the bluff bodies, thereby, their aerodynamic behaviors.

According to the literature review, it is known that the surfaces of bluff bodies can significantly influence their aerodynamic behaviors. Metasurfaces have been widely used in many disciplines and diverse engineering applications, such as acoustics [60,61], electronics [62,63], and material science [64]. Ma et al. [65] reported a novel acoustic metasurface to achieve impedance matching and realize no reflection on the incident waves. Wu et al. [66] proposed a programmable metasurface that could deflect the terahertz (THz) beam and open a novel route for THz communication. Shalaginov et al. [67] provided a critical active control algorithm for optical metasurface, which enabled some optical devices to realize unprecedented new functions.

Inspired by the abovementioned studies, this paper investigates the aerodynamic responses of several cylinder bluff bodies with etched concave metasurface patterns. The paper is structured as follows. Section 2 introduces the structure of the proposed FIV energy harvester and a general single-degree-of-freedom (SDOF) model to capture its dynamics. The experimental setup and the physical prototypes are presented in Section 3. The simulated lift and drag coefficients of different bluff bodies are presented in Section 4. Section 5 compares and discusses the experimental and theoretical results. The effects of electrical parameters on energy harvesting performance are discussed in Section 6. Conclusions drawn from this work are summarized in Section 7.

2. Theoretical model

2.1. Lumped parameter model

For a traditional VIVPEH, as shown in Fig. 1, its fundamental resonance will be prominently activated at low wind speeds, while higher-order resonances have negligible contributions. Hence, only the fundamental mode of the VIVPEH will be considered for simplicity. Based on Euler's beam theory [68], the governing equation of the piezoelectric beam can be written as:

$$\ddot{Z}(t) + 2\xi\omega_n\dot{Z}(t) + \omega_n^2 Z(t) + \alpha_e V(t) = f_{VIV}(t) \tag{1}$$

where $Z(t)$ is the model coordinate, $\dot{Z}(t)$ and $\ddot{Z}(t)$ are the model velocity and the modal acceleration, respectively. ξ is the damping ratio, ω_n is the natural angular frequency of the fundamental resonance. α_e is the modal electromechanical coupling coefficient. $f_{VIV}(t)$ is the vortex-induced aerodynamic force, which can be further expressed as:

$$f_{VIV}(t) = \frac{1}{2}\rho D U^2 L_0 C_L \Phi(L_c) - \frac{1}{2}\rho D U L_0 C_D^{mean}[\Phi(L_c)]^2 \dot{Z}(t) \tag{2}$$

where $C_L = q(t)C_{L0}/2$ is the fluctuating lift force coefficient. C_{L0} is the amplitude of the fluctuating lift force coefficient and C_D^{mean} is the mean drag coefficient. $\Phi(L_c)$ is the modal shape of the fundamental resonance. ρ is the air density. D is the characteristic diameter of the bluff body. A broadband piezo-electromagnetic hybrid energy harvester under combined vortex-induced and base excitations U and L_0 are the fluid velocity and bluff body length, respectively.

In 2004, Facchinetti et al. [69] proposed to use the van der Pol wake

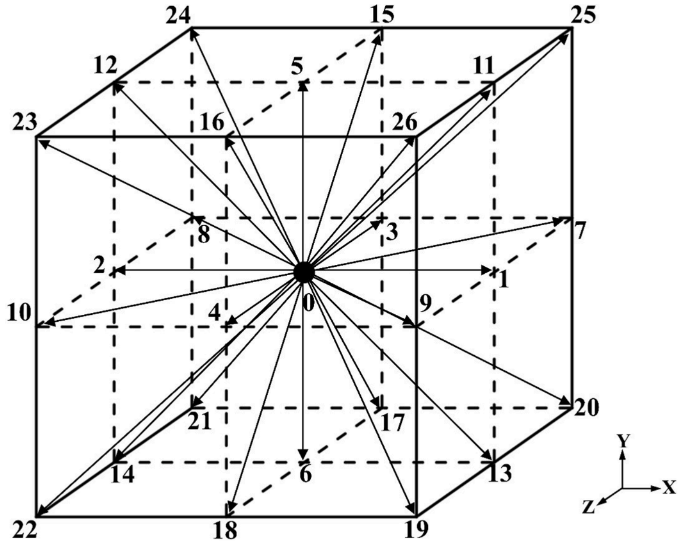

Fig. 3. D3Q27 discrete velocity model of the LBM. The velocity space is discretized into 27 discrete velocities.

oscillator equation to model the dynamics of the near wake generated behind the bluff body.

$$\ddot{q}(t) + \lambda\omega_V\left[q^2(t) - 1\right]\dot{q}(t) + \omega_V^2 q(t) = \frac{A}{D}\Phi(L_c)\ddot{Z}(t) \tag{3}$$

where $q(t)$ describes the near-wake vortex motion. It is a variable related to the averaged transverse component of the flow [70] and proportional to the transverse velocity of the near-wake fluid [71]. ω_V is the vortex shedding angular frequency, which can be calculated by $\omega_V = 2\pi S_t U/D$. λ and A are the constants equaling 0.3 and 12, respectively [69].

Suppose the external load of the VIVPEH is a simple resistor R_L and the current flowing through the resistor is $I_p(t)$, as shown in Fig. 2, one can write the governing equation of the electrical domain by using Kirchhoff's current law.

$$\alpha_e\dot{Z}(t) - C_p\dot{V}(t) = \frac{V(t)}{R_L} \tag{4}$$

Combining Eqs.(1) - (3) and eliminating the term $\Phi(L_c)$, the governing equations of the SDOF model [72] of the VIVPEH can be obtained:

$$M_{eff}\ddot{z}(t) + \left[\frac{1}{2}\rho D U L_0 C_D^{mean} + C_{eff}\right]\dot{z}(t) + K_{eff}z(t) + \theta V(t) = \frac{1}{4}\rho C_{L0} D L_0 U^2 q(t) \tag{5}$$

$$\ddot{q}(t) + \lambda\omega_V\left[q^2(t) - 1\right]\dot{q}(t) + \omega_V^2 q(t) = \frac{A}{D}\ddot{z}(t) \tag{6}$$

$$\theta\dot{z}(t) - C_p\dot{V}(t) = \frac{V(t)}{R_L} \tag{7}$$

where $M_{eff} = 1/\Phi^2(L_c)$, $C_{eff} = 1/\Phi^2(L_c)$, $K_{eff} = 1/\Phi^2(L_c)$, $\theta = \alpha_e/\Phi(L_c)$, $z(t) = \Phi(L_c)Z(t)$, C_p is the clamped capacitance of the piezoelectric transducer and θ is the electromechanical coupling coefficient.

By introducing the intermediate variable Y:

$$Y = \begin{Bmatrix} y_1 \\ y_2 \\ y_3 \\ y_4 \\ y_5 \end{Bmatrix} = \begin{Bmatrix} z(t) \\ \dot{z}(t) \\ V(t) \\ q(t) \\ \dot{q}(t) \end{Bmatrix} \tag{8}$$

Eqs.(5) - (7) can be cast in the state-space representation:

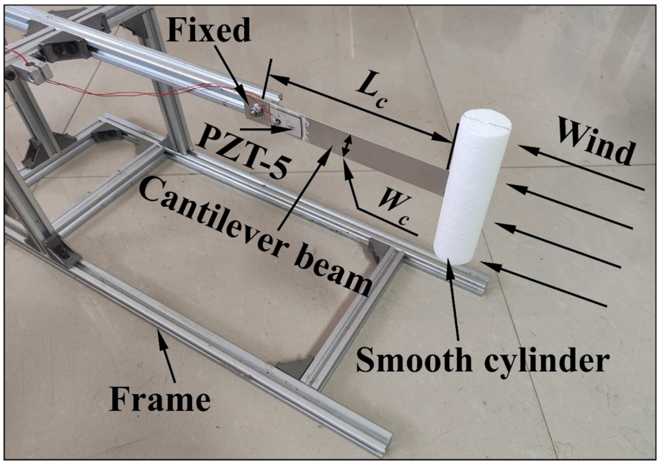

Fig. 5. The physical prototype of the baseline VIVPEH using a smooth cylinder bluff body. The VIVPEH is mounted on a metal frame, which will be placed in a wind tunnel in the experimental test.

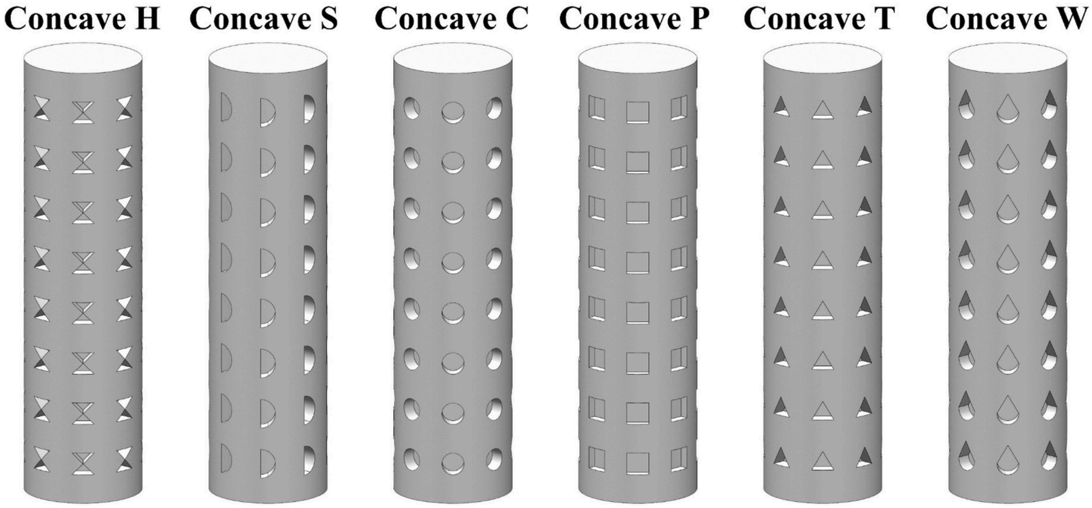

Fig. 4. Bluff bodies etched with different metasurface patterns. From left to right, they are concave hourglass (concave H), concave semicircle (concave S), concave circle (concave C), concave prism (concave P), concave triangle (concave T), and concave waterdrop (concave W) metasurface patterns.

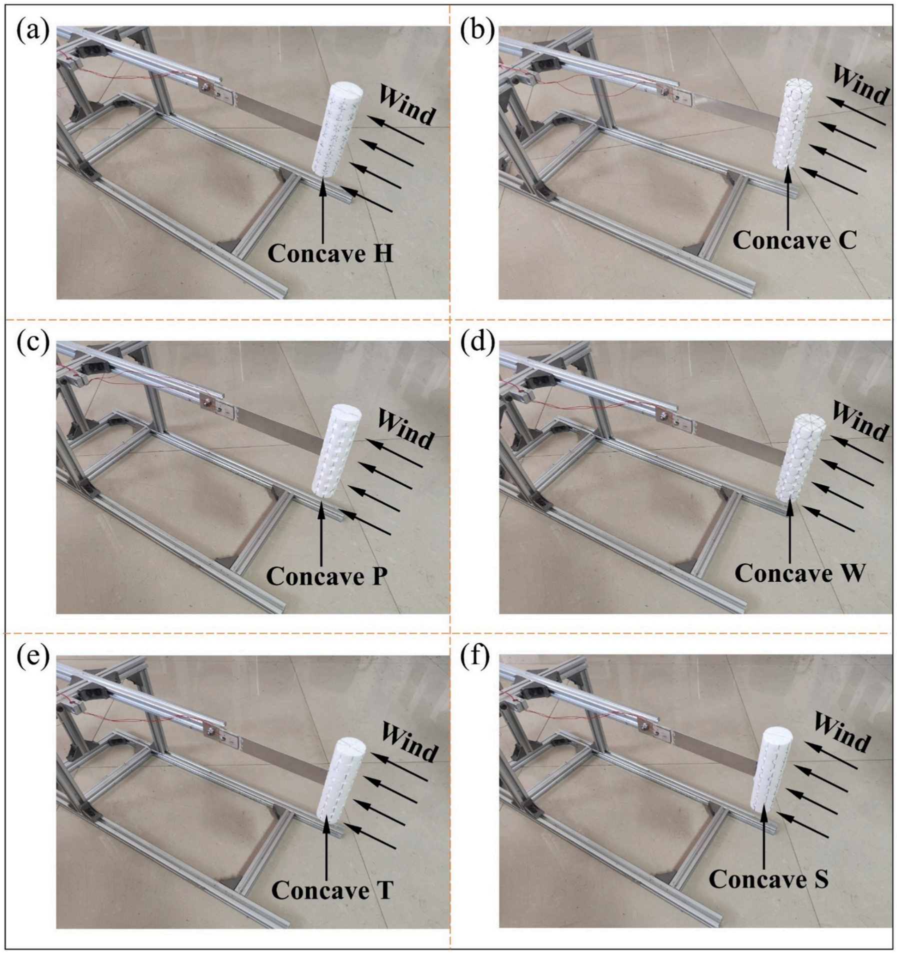

Fig. 6. Physical prototypes of the proposed VIVPEHs using cylinder bluff bodies etched with different metasurface patterns on their surfaces: (a) concave hourglass (H); (b) concave circle (C); (c) concave prism (P); (d) concave waterdrop (W); (e) concave triangle (T); (f) concave semicircle (S).

$$\dot{Y} = \left\{ \begin{array}{c} \dot{z}(t) \\ \ddot{z}(t) \\ \dot{V}(t) \\ \dot{q}(t) \\ \ddot{q}(t) \end{array} \right\}$$
$$= \left\{ \begin{array}{c} y_2 \\ \frac{1}{M_{eff}}\left[\frac{1}{4}\rho C_{L0} D L_0 U^2 y_4 - \theta y_3 - K_{eff} y_1 - \left(\frac{1}{2}\rho D U L_0 C_D^{mean} + C_{eff}\right) y_2\right] \\ \frac{\theta y_2}{C_p} - \frac{y_3}{C_p R_L} \\ y_5 \\ \frac{A}{D M_{eff}} \left[\begin{array}{l} \frac{1}{4}\rho C_{L0} D L_0 U^2 y_4 - \theta y_3 - K_{eff} y_1 \\ -\left(\frac{1}{2}\rho D U L_0 C_D^{mean} + C_{eff}\right) y_2 \end{array} \right] - \lambda \omega_V \left(y_4^2 - 1\right) y_5 - \omega_V^2 y_4 \end{array} \right\} \tag{9}$$

One can easily solve the ordinary differential equations in Eq. (9) using numerical approaches, such as the Runge-Kutta method.

2.2. D3Q27 model

This section introduces the D3Q27 model used in CFD simulation based on Lattice Boltzmann method (LBM). Instead of the traditional commercial software ANSYS Fluent which adopts the finite element method (FEM), the CFD platform XFlow which adopts the Lattice-Boltzmann method, is utilized to simulate the flow fields. LBM is eminently suitable for simulating the aerodynamics of structures with complicated geometries, and XFlow provides an excellent solution for large-scale CPU/GPU parallel computing. Moreover, compared with the traditional CFD method, which needs to solve the complex second-order nonlinear Navier-Stokes equation (NS equation), the Boltzmann transport equation solved by LBM is a more straightforward first-order equation [73]:

$$f_n(\overrightarrow{r} + e_n dt, t + dt) - f_n(\overrightarrow{r}, t) = \Omega_n(f_0, ..., f_b), n = 0, 1, ..., b \tag{10}$$

where $f_n(\overrightarrow{r}, t)$ is the particle distribution function; the vector $\overrightarrow{r}$ can be futher expanded as $\overrightarrow{r} = xi + yj + zk$, where *i, j, k* are the unit vectors corresponding to *x, y* and *z* axes, respectively; e_n is the particle velocity component in *n*th direction; *dt* is the time step and Ω_n is the collision operator; $b = 26$ (*b* starts from 0) indicates that the velocity space is discretized into 27 discrete velocities, as shown in Fig. 3. Thus, the model is referred to as the D3Q27 model [74]. The required mathematical processing is much simpler than FEM.

Solving the Boltzmann equation is difficult because of the complexity of the collision term. Fortunately, Bhatnagar et al. [75] introduced a simplified model for describing the collision process and significantly reduced the difficulty of solving the Boltzmann transport equation. They expressed the collision operator as:

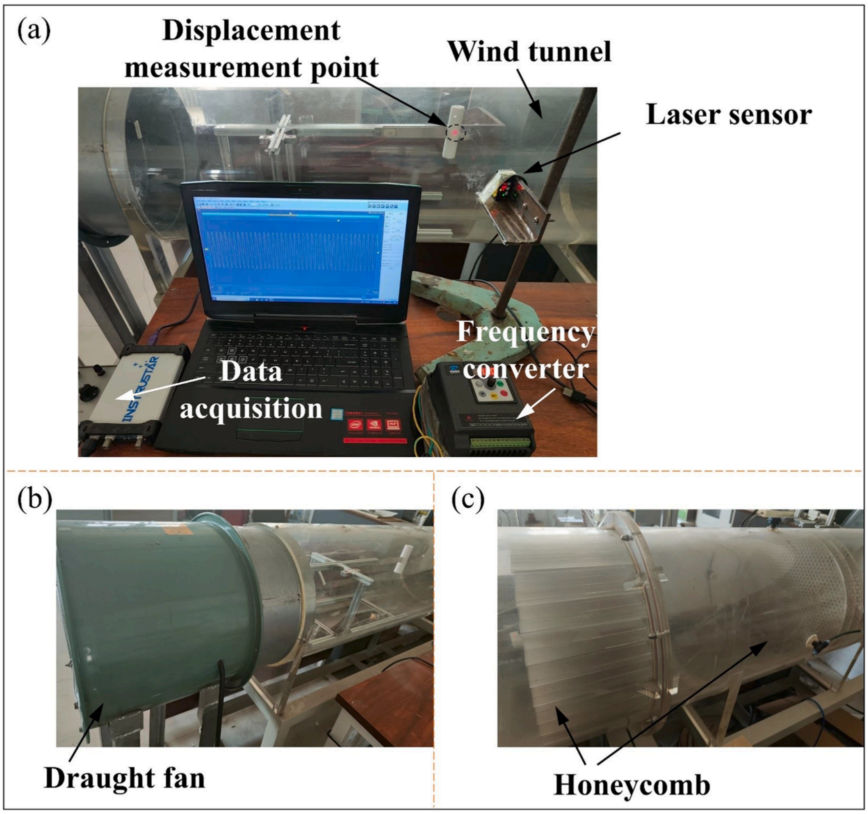

Fig. 7. (a) The whole experiment setup, including the wind tunnel, the wind speed controller (frequency converter), and the data acquisition system; (b) the enlarged view of the draught fan; (c) the enlarged view of the honeycomb baffle plates.

Table 1
Physical parameters of the incoming flow.

Physical parameters	Units	Values
Molecular weight	kg/mol	28.996
Temperature	K	288
Density	kg/m^3	1.225
Kinetic viscosity	Pa·s	1.7894×10^{-5}
Thermal conductivity	W/(m·K)	0.0243
Specific heat capacity	J/(kg·K)	1006.43

$$\Omega_n^{BGK} = \frac{1}{\tau}\left(f_n^{eq} - f_n\right) \tag{11}$$

where τ is the relaxation time, and the local equilibrium distribution function f_n^{eq} further expands as:

$$f_n^{eq} = \rho\omega_n\left[1 + \frac{e_{n\alpha}u_\alpha}{c_s^2} + \frac{u_\alpha u_\beta}{2c_s^2}\left(\frac{e_{n\alpha}e_{n\beta}}{c_s^2} - \delta_{\alpha\beta}\right)\right] \tag{12}$$

where $\vec{u}$ is the macroscopic flow velocity vector, and ρ is the macroscopic density; $\sum_{n=0}^{n=b}\omega_n = 1$ are weighting constants to ensure the conservation of isotropy; the subscripts α and β indicate different spatial components of the vectors; δ is the Kronecker delta. c_s is the sound speed that can be written as $c_s/c = 1/\sqrt{3}$ in the D3Q27 model, where $c = dx/dt$ is the lattice speed, and dx is the lattice spacing.

The macroscopic density and linear momentum can be formulated as:

$$\rho = \sum\nolimits_{n=0}^{n=b} f_n = \sum\nolimits_{n=0}^{n=b} f_n^{eq} \tag{13}$$

$$\rho\vec{u} = \sum\nolimits_{n=0}^{n=b} f_n e_n = \sum\nolimits_{n=0}^{n=b} f_n^{eq} e_n \tag{14}$$

and the macroscopic pressure for incompressible fluid can be obtained by simply manipulating Eq. (14):

$$p = \rho c_s^2 = \frac{1}{3}\left(\frac{dx}{dt}\right)^2 \sum\nolimits_{n=0}^{n=b} f_n = \frac{1}{3}\left(\frac{dx}{dt}\right)^2 \sum\nolimits_{n=0}^{n=b} f_n^{eq} \tag{15}$$

3. Physical prototypes and experimental setup

We designed several representative metasurface patterns shown in Fig. 4 and etched them on the surfaces of cylinder bluff bodies. According to the micro-shapes, they are referred to as the concave hourglass (concave H), concave semicircle (concave S), concave circle (concave C), concave prism (concave P), concave triangle (concave T), and concave waterdrop (concave W) metasurface patterns, respectively. The etching depth of the patterns is 4 mm, and the characteristic length L_1 of the micro-shapes is 6 mm. The topmost array of micro-shapes situates 11 mm below the top surface of the cylinder. The distance between the centers of the adjacent arrays of micro-shapes is 14 mm. Sixty-four micro-shapes are regularly distributed on each bluff body.

The conventional VIVPEH equipped with a cylinder bluff body, as shown in Fig. 5, is referred to as the baseline model and will be used for comparison. The proposed metasurface patterns are etched on the cylinder bluff bodies with the same geometric dimensions. Fig. 6 shows the six experimental prototypes. The bluff bodies etched with different metasurfaces have different masses. Auxiliary weights are added to guarantee they have the same mass for a fair comparison in later studies, and the masses of different bluff bodies M_2 are unified to 1.7 g.

The cantilever beam with dimensions of $L_c \times W_c \times T_c = 170 \times 25 \times 0.5$ mm^3 is made of aluminum. The frame is made of aluminum alloy. The Expanded Polystyrene (EPS) made bluff body has a length of 12 cm and a diameter of 32 mm. A PZT-5 patch with dimensions of $L_p \times W_p \times T_p = 30 \times 20 \times 0.5$ mm^3 is bonded on the cantilever beam near its root

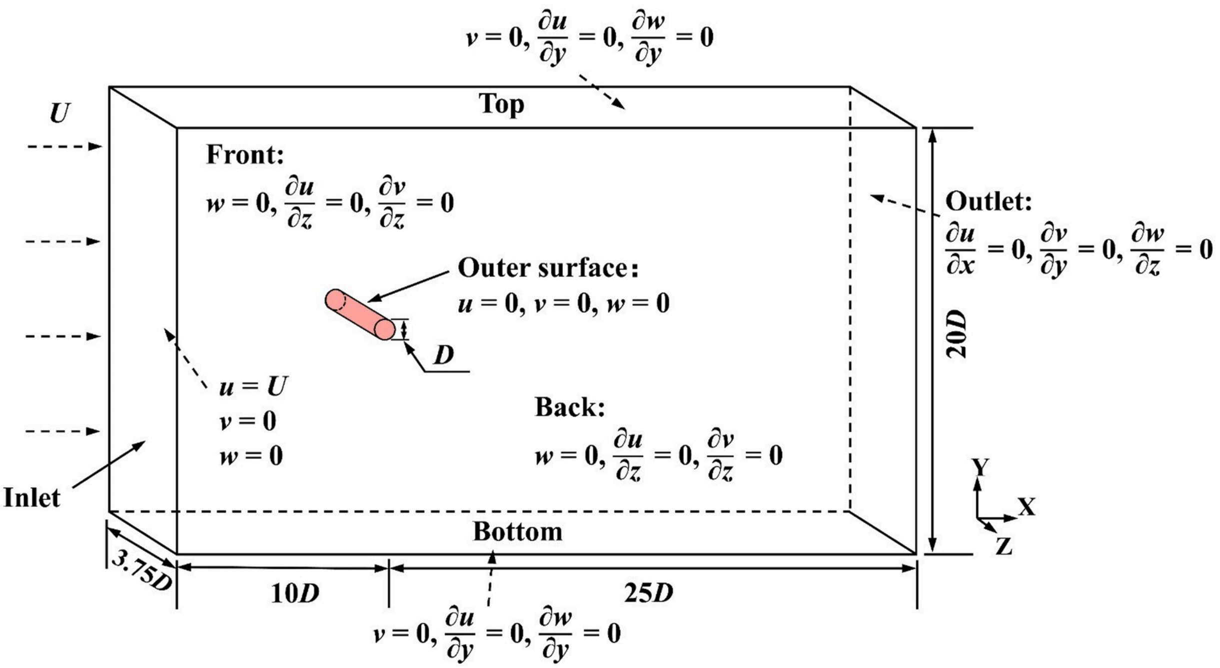

Fig. 8. Scheme of the computational domain and the boundary conditions. The left and right ends are, respectively, set as the inlet and outlet. Neumann and Dirichlet boundary conditions are applied to the top and bottom boundaries.

Table 2
C_D^{mean} and C_L^{rms} computed using different lattice sizes.

Lattice size	C_D^{mean}	$\mathrm{C}_{L^r}^{ms}$
Coarse	1.246	0.156
Normal	1.192	0.235
Fine	1.194	0.220

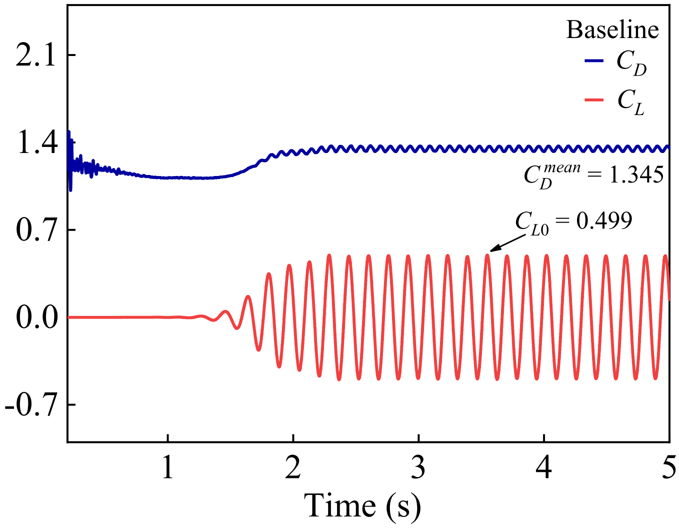

Fig. 9. Time-history C_L and C_D for the cylinder bluff body with smooth surface.

using acrylic acid. A small gap $L_g = 3$ mm shown in Fig. 1 is to prevent damage of the PZT-5 patch due to the stress concentration at the clamped end. The bluff body is assembled with the cantilever beam by glue. The total mass of the piezoelectric cantilever beam M_1 (including the cantilever beam, the PZT-5 patch, and the acrylic acid) is 10.4 g.

As shown in Fig. 7(a), the VIVPEH in the test is placed in a 0.4 m diameter wind tunnel. Two honeycomb baffle plates are installed to stabilize the incoming wind. The voltage output produced by the VIVPEH is measured by a dual-channel digital oscilloscope (ISDS220B), and the displacement of the bluff body is measured by a laser displacement sensor (Panasonic HG-C1400). The wind speed U in the wind tunnel is gauged by a hot-wire anemometer (Testo Co., USA). A draught fan generates a wind flow. A frequency converter controls the wind speed by changing the rotation frequency f. The relationship between U and f follows $U = 0.137f + 0.18$. The baseline VIVPEH attached with a smooth cylinder bluff body was tested first. The other prototypes were tested successively. In the following comparison study, the bluff body was replaced during the tests, while the cantilever beam and the bonded piezoelectric transducer were untouched.

4. CFD setup and simulation results

The influence of the lattice number on the convergence of simulation results was studied first. The simulation result is deemed converged when the change of the lattice number has little effect on the simulation results. We took a smooth cylinder bluff body as an example and placed it in a wind flow with the speed of $U = 2.509$ m/s. The cylinder diameter (D) is 32 mm, and the length (L_0) is 120 mm. Detailed information on the wind flow is listed in Table 1. The Reynolds number (R_e) can be determined to be 5900, which indicates a laminar flow condition for the boundary layer. Fig. 8 shows the scheme of the CFD computational domain and illustrates how the boundary conditions are implemented.

The top and bottom boundaries are separated by 20D. Three global lattice scales (0.0344D, 0.0313D, 0.0297D), are referred to as coarse, normal, and fine sizes, respectively. The lattice resolution near the bluff body is 4 times that of the global lattice. The lattice numbers of the coarse, normal, and fine models are 1176,038, 1496,800 and 1761,596, respectively. The time step size is set as ‘Fixed-Automatic’. The built-in Smagorinsky model provided in XFlow is adopted for Large Eddy Simulation (LES) since it exhibits good accuracy in dealing with aerodynamic characteristics of bluff bodies [76–78].

The mean value of the drag coefficient C_D^{mean} and the root mean square (RMS) value of the lift coefficient C_L^{rms} calculated by the coarse, normal, and fine models are listed in Table 2. It can be noted that both C_D^{mean} and C_L^{rms} converge as the lattice size reduces. The normal lattice

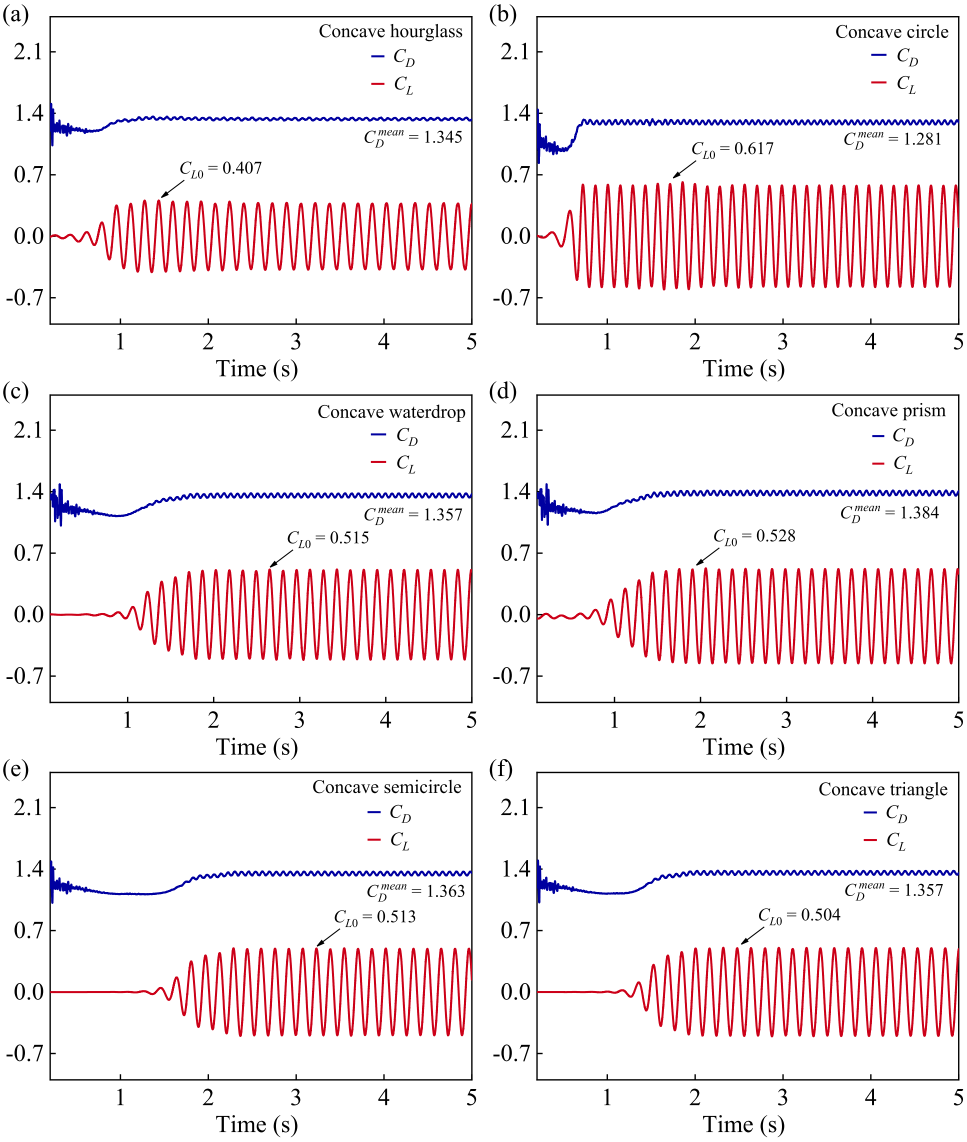

Fig. 10. Time-history C_L and C_D for bluff bodies with different surface conditions: (a) concave hourglass; (b) concave circle; (c) concave waterdrop; (d) concave prism; (e) concave semicircle; (f) concave triangle.

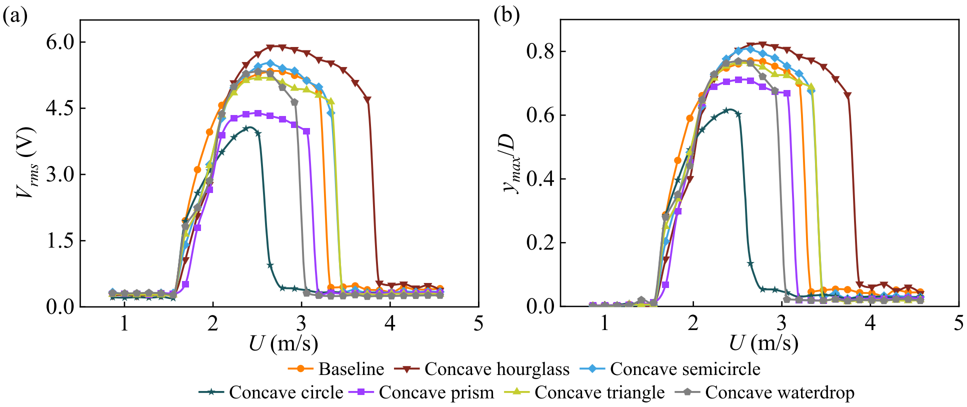

Fig. 11. Experimentally measured RMS output voltage V_{rms} and post-processed dimensionless displacement amplitudes y_{max}/D of the energy harvesters equipped with different bluff bodies.

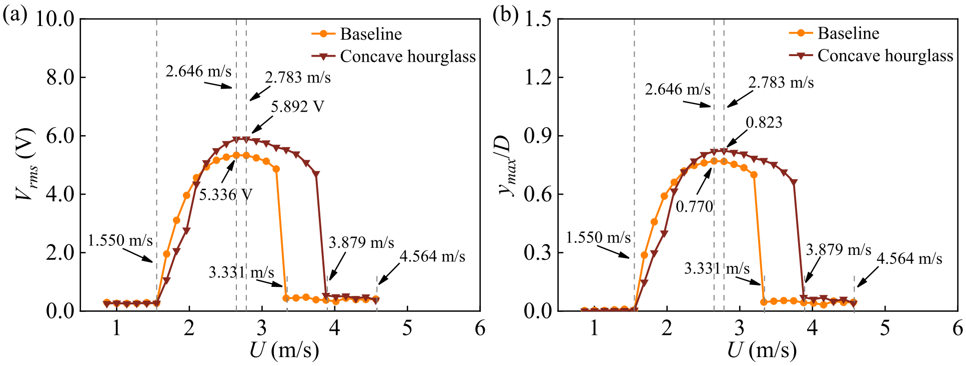

Fig. 12. Comparison between the experimental results of the baseline model and the concave H model: (a) RMS voltage output responses; (b) dimensionless displacement responses.

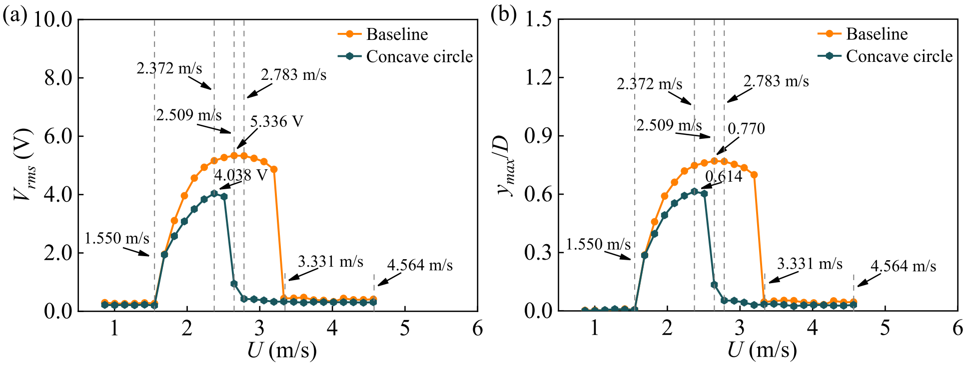

Fig. 13. Comparison between the experimental results of the baseline model and the concave C model: (a) RMS voltage output responses; (b) dimensionless displacement responses.

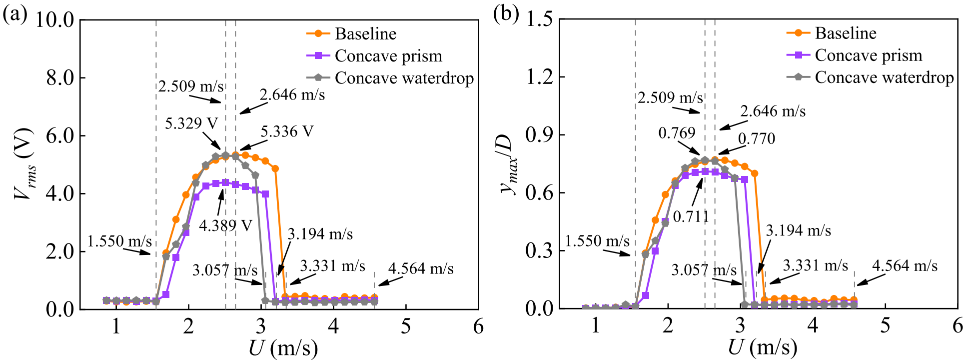

Fig. 14. Comparison between the experimental results of the baseline model and the concave P & W models: (a) RMS voltage output responses; (b) dimensionless displacement responses.

size (0.0313D) is adopted in the simulations to compromise the computational efficiency and accuracy.

The normal lattice size was first used to simulate the aerodynamics of the cylinder bluff bodies with smooth surface, concave H, concave C, concave P, concave W, and concave S metasurface patterns at $U = 1.143$ m/s. The time-history C_D and C_L are shown in Figs. 9 and 10. These values can then be used in the general lumped parameter model presented in Section 2.1 for simulating their wind energy harvesting performance.

5. Results and discussions

5.1. Experimental results

Fig. 11 presents the experimental results of the VIVPEHs equipped with different metasurface etched bluff bodies. It can be observed that, as compared to the baseline, the ones etched with concave H, C, P, and W metasurface patterns exhibit conspicuously different aerodynamic behaviors. Some metasurface patterns can help enhance VIV by enlarging the bandwidth (i.e., lock-in region) and increasing the vibration magnitude. In contrast, others can suppress VIV by narrowing the bandwidth and repressing the magnitude. The aerodynamics of the S and T patterns etched bluff bodies are consistent with the baseline model since their curves almost overlap.

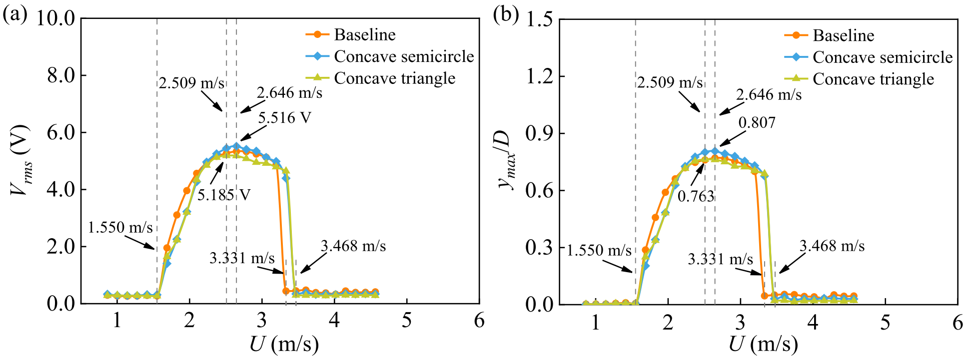

Fig. 15. Comparison between the experimental results of the baseline model and the concave S & T models: (a) RMS voltage output responses; (b) dimensionless displacement responses.

Table 3
The lumped parameters of the experimental prototype.

Lumped parameters	Units	Values
M_{eff}	g	4.151
C_{eff}	N/(m/s)	0.0072
K_{eff}	N/m	14.58
ω_n	rad/s	59.26
ξ	/	0.0147
θ	N/V	7.9×10^{-6}
C_p	F	1.875×10^{-8}

Table 4
The aerodynamic coefficients of bluff bodies etched with different metasurface patterns.

Concave patterns	C_D^{mean}	C_{L0}	S_t
Baseline	1.345	0.499	0.131
Concave H	1.335	0.407	0.119
Concave C	1.281	0.617	0.172
Concave W	1.357	0.515	0.138
Concave P	1.384	0.528	0.141
Concave S	1.363	0.513	0.132
Concave T	1.357	0.504	0.132

We classify the metasurface patterns into three categories according to their effects on the aerodynamics of the bluff body and investigate each category separately. Fig. 12 compares the responses of the baseline model and the one etched with the concave H metasurface pattern, which is referred to as the concave H model hereafter for brevity, as well as for the other models. The maximum RMS voltage output of the baseline model is 5.336 V, the maximum dimensionless displacement amplitude (y_{max}/D) is 0.770, and the effective working bandwidth is 1.550 ~ 3.879 m/s. The maximum RMS voltage output of the concave H model is 5.892 V, the maximum dimensionless displacement amplitude is 0.823, and the effective working bandwidth is 1.550 ~ 3.331 m/s. In terms of the maximum RMS voltage output, the maximum dimensionless displacement amplitude, and the effective working bandwidth, the concave H model demonstrates improvements of 10.42%, 6.44%, and 30.77%, respectively.

In contrast, etching the concave C metasurface pattern on the bluff body suppresses VIV. The experimental results of the baseline model and the concave C model are compared in Fig. 13. The maximum RMS voltage output, the maximum y_{max}/D, and the effective working bandwidth of the concave C model are, respectively, 4.038 V, 0.614, and 1.550 ~ 2.783 m/s. Compared to the baseline model, the corresponding parameters of the concave C model decreased by 24.33%, 20.26%, and 44.44%, respectively.

Etching concave P and W metasurface patterns on the bluff body also suppress VIV but more weakly than the concave C metasurface pattern. The experimental results of the concave P and W models are presented in Fig. 14. The maximum RMS voltage outputs of the concave P and W models are 4.389 V and 5.329 V, respectively, indicating a decrease of 17.75% and 0.13% compared to the baseline model. Their maximum dimensionless displacement amplitudes are 0.711 and 0.769, respectively, suggesting a decline of 7.66% and 0.13%, respectively. And their effective working bandwidths are 1.550 ~ 3.194 m/s and 1.550 ~ 3.057 m/s, respectively, manifesting a shrinkage of 7.69% and 15.38%, respectively.

Etching metasurface patterns on bluff bodies does not necessarily modify their aerodynamics. Fig. 15 presents experimental results of the concave S and T models and reveals that the two metasurface patterns almost did not result in any appreciable change. The maximum RMS voltage output of the concave S model diminishes by just 3.37% compared to the baseline model. The decrease in the maximum dimensionless amplitude of the concave S model is around 4.81%. The declines of the maximum RMS voltage and maximum dimensionless amplitude of the concave T model are even smaller, respectively, 2.83% and 0.91%. The effective working bandwidths of the concave S and T models are the same, 1.550 ~ 3.468 m/s, which indicates a decrement of 7.69%.

5.2. *Theoretical model validation*

The experimental results are also used to validate the theoretical model (Eqs.(5) - (7)). The equivalent mass of the VIVPEH can be approximately calculated by $M_{eff} = 33/140 \times M_1 + M_2$. The damping coefficient C_{eff} and the stiffness K_{eff} can be calculated as $C_{eff} = 2\xi\omega_n M_{eff}$ and $K_{eff} = \omega_n^2 M_{eff}$. The natural angular frequency ω_n equals $2\pi f_n$. Both f_n and ξ can be experimentally determined via a free decay test. The piezoelectric transducer is open-circuited. The equivalent lumped parameters of the physical prototypes are listed in Table 3. The aerodynamic coefficients of the bluff bodies with and without surface treatments are listed in Table 4.

Fig. 16 shows the theoretically predicted and experimental obtained RMS voltage outputs and the dimensionless displacement amplitudes of different VIVPEH prototypes. Overall speaking, all the theoretical results generally match the experimental results. The discrepancies between them may arise due to the following reasons. First, the simplified SDOF model is not sufficiently accurate to capture the dynamics of the VIVPEHs. Second, minor errors may exist in the measurement for determining the equivalent lumped parameters. Third, the CFD simulation results could not exactly reveal the aerodynamics of the bluff bodies in the practical tests. Moreover, the equations of the aerodynamic forces applied to the bluff bodies in the theoretical models are obtained empirically.

As can be found in Table 4, the Strouhal number S_t of the bluff body etched with the concave H pattern is smaller than that of the baseline

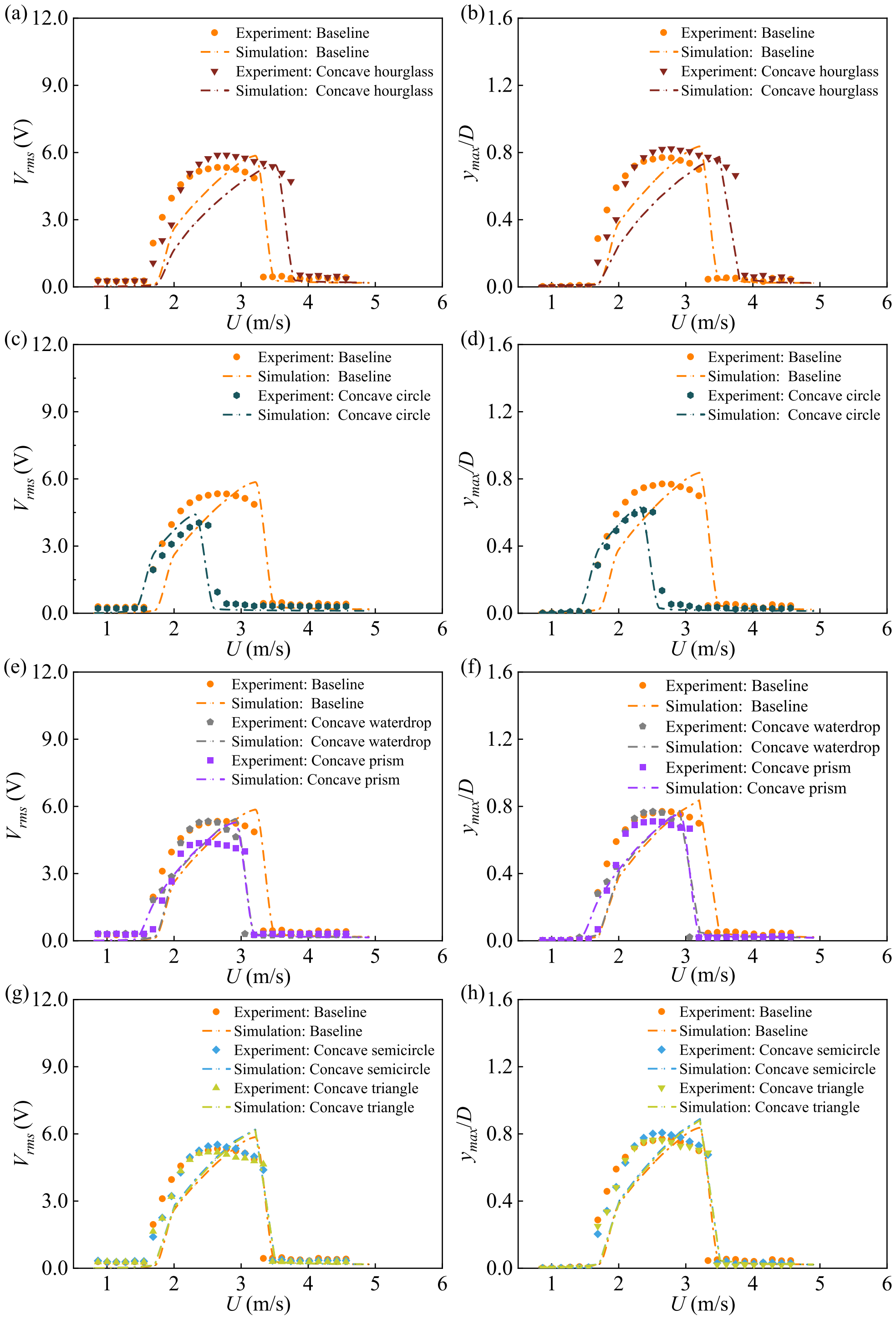

Fig. 16. Comparison of the experimental and theoretical results of the dynamic responses (i.e., RMS voltage output and the dimensionless displacement amplitudes) of the VIVPEHs. (a) concave H model versus baseline on voltage; (b) concave H model versus baseline on displacement; (c) concave C model versus baseline on voltage; (d) concave C model versus baseline on displacement; (e) concave W & P models versus baseline on voltage; (f) concave W & P models versus baseline on displacement; (g) concave S & T models versus baseline on voltage; (h) concave S & T models versus baseline on displacement.

bluff body, but the S_t values of the buff bodies etched with concave C, W, and Q patterns are larger than the baseline. The S_t of the bluff body etched with the concave S pattern is almost the same as the baseline. These results imply that smaller S_t provides a sign of enhancing VIV, while larger S_t suppresses VIV. A further explanation can be obtained by revisiting the definition of the Strouhal number S_t and the mechanism of VIV.

The Strouhal number S_t is defined as $S_t = f_s D/U$. It is a dimensionless proportionality constant that describes the relationship between the vortex shedding frequency f_s, the characteristic length of the bluff body D, and the flow velocity U. When the fluid flows around a bluff body with elastic support, due to the boundary layer separation effect, vortices periodically occur in the wake behind the bluff body, producing an asymmetric but periodic pressure field. Hence, an alternating aerodynamic force will be applied to the bluff body and drives the VIVPEH to vibrate. When the vortex shedding frequency gets closer to the natural frequency of the VIVPEH, structural resonance will take place, and the displacement amplitude will increase significantly; then, the vortex shedding frequency will be 'locked' within a specific range of flow speed.

As the wind speed keeps increasing, the vortex shedding frequency drifts away from the resonant frequency; thus, the system vibration

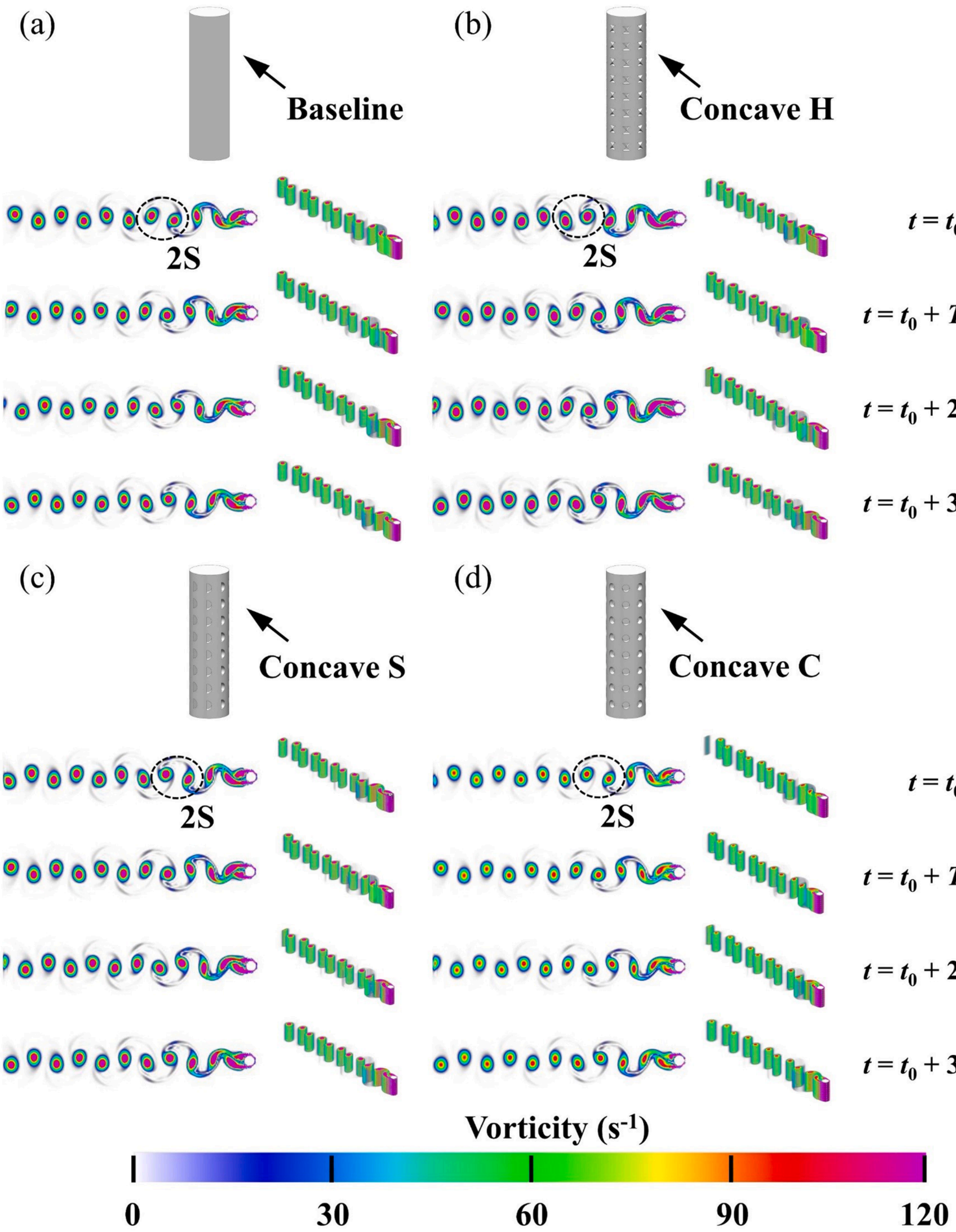

Fig. 17. Vorticity contours at a period of different bluff bodies for $U = 2.372$ m/s: (a) the baseline bluff body (a smooth cylinder); (b) the bluff body etched with the concave H pattern; (c) the bluff body etched with the concave S pattern; (d) the bluff body etched with the concave C pattern.

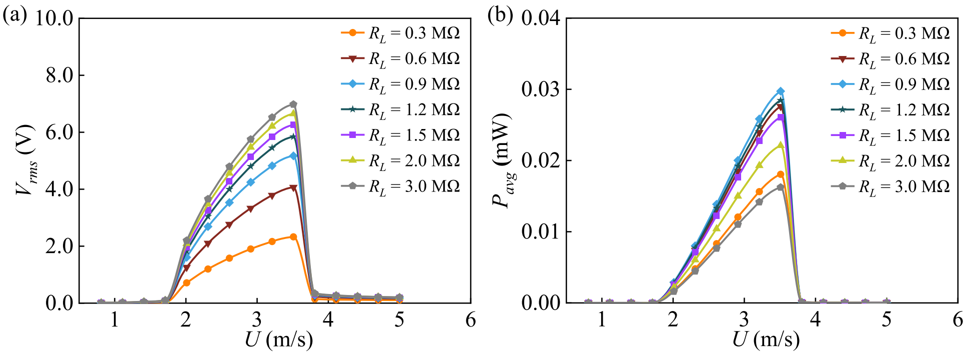

Fig. 18. The variation of (a) V_{rms} and (b) P_{avg} with the change of wind speed under different load resistances.

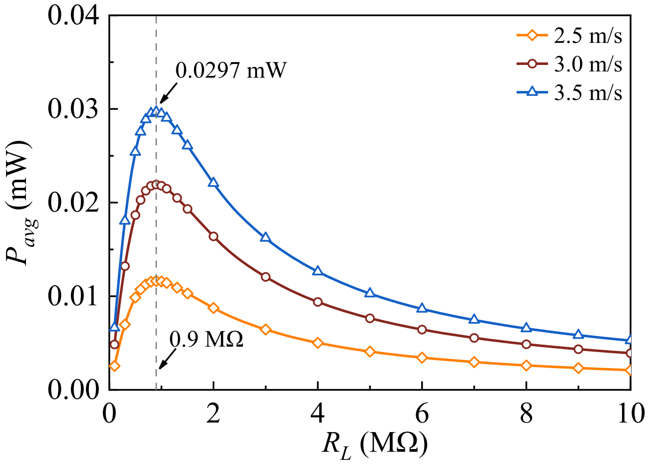

Fig. 19. The variation of P_{avg} with the change of load resistance under different wind speeds. The optimal resistance is identified to be 0.9 MΩ.

eventually terminates. By combining the data in Table 4 and the responses in Fig. 16(c) and (d), one knows that a larger S_t indicates a larger increase rate of the vortex shedding frequency, making it more easily to exceed the system resonant frequency. That explains why the concave S model with a larger S_t has a much narrow effective working bandwidth. The results in Fig. 16(a) & (b) and the S_t of the concave H bluff body in Table 4 indicate that for a smaller S_t, the vortex shedding frequency catches up with the resonant frequency slowly. Similar conclusions and explanations can be obtained by interpreting the results in other subplots of Fig. 16 with the help of the data in Table 4. In brief, by comparing the Strouhal number S_t with the baseline, one can fast predict whether VIV will be enhanced or suppressed: a smaller S_t enhances VIV by enlarging the effective working bandwidth, but a larger S_t brings the opposite effect by reducing the effective working bandwidth and suppressing VIV magnitude.

5.3. *Interpretation of CFD results*

To illustrate the effects of different metasurfaces, Fig. 17 presents CFD simulated vortex shedding processes over a cycle. All the four vorticity contours show the typical 2S (Single pattern) shedding pattern: only one vortex will be generated in the wake region of a half vortex-induced vibration period, and two independent vortices will be generated in a complete vortex-induced vibration period. The vortices behind the bluff body etched with the concave H pattern are more intense, and the vortex strength within one period (Fig. 17(b)) is larger than the baseline (Fig. 17(a)). Its vortex strength does not significantly decrease after shedding off the bluff body. However, the vortex strength behind the bluff body etched with the concave C pattern is remarkably reduced (Fig. 17(d)). The vortex strength within a stable period is much smaller than that of the baseline bluff body. Regarding the bluff body etched with the concave S pattern, its vorticity contour plot (Fig. 17(c)) is almost the same as that of the baseline bluff body (Fig. 17(a)).

The vorticity contour plots obtained by CFD simulations vividly reveal the effects of the metasurface patterns on the aerodynamics of the bluff bodies. The flow field at the wake of the bluff body changes more violently due to the introduction of the concave H pattern, accompanied by a remarkable change of the wake pressure. Consequently, larger vibrations can be induced to enhance the energy harvesting performance. However, the existence of the concave C pattern mitigates the change of the flow field in the wake of the bluff body, leading to a weaker pressure change, which is beneficial to suppressing VIV. The vorticity contour plots of other metasurface pattern etched bluff bodies can be simulated and interpreted in a similar way. For brevity, we only picked the three typical ones.

6. Parametric studies

As an electromechanical system, electrical system parameters, such as the load resistance R_L and electromechanical coupling strength ${k_e}^2$, also have significant effects on the performance of wind energy harvesters. This section investigates the influence of R_L and ${k_e}^2$ on the energy harvesting performance. The following formulas respectively define the average power and electromechanical coupling strength:

$$P_{avg} = \frac{V_{rms}^2}{R_L} \tag{16}$$

$$k_e^2 = \frac{\theta^2}{C_p K_{eff}} \tag{17}$$

The concave H model is taken as an example to conduct the following parametric study. Fig. 18 shows the variation of RMS voltage output and average power with the change of wind speed under different load resistances. As can be found in Fig. 18(a), V_{rms} increases with the increase of R_L. But according to the maximum power theory, P_{avg} cannot grow infinitely, and there must be a maximum value. Fig. 18(b) shows that with increasing R_L, P_{avg} first increases and then decreases. The optimal load resistance R_{opt} is estimated between 0.6 and 1.2 MΩ.

Fig. 19 shows the variation of P_{avg} in response to the change of the load resistance under different wind speeds. Regardless of the wind speed, with the increase of the load resistance, the average power always increases first, then decreases. The maximum average power is obtained at $R_L = 0.9$ MΩ. Hence, we could deduce that the optimal load is $R_{opt} = 0.9$ MΩ. Moreover, we notice that the optimal resistance is the same under different wind speeds. The maximum average power obtained at $U = 3.5$ m/s and $R_{opt} = 0.9$ MΩ is 0.0297 mW.

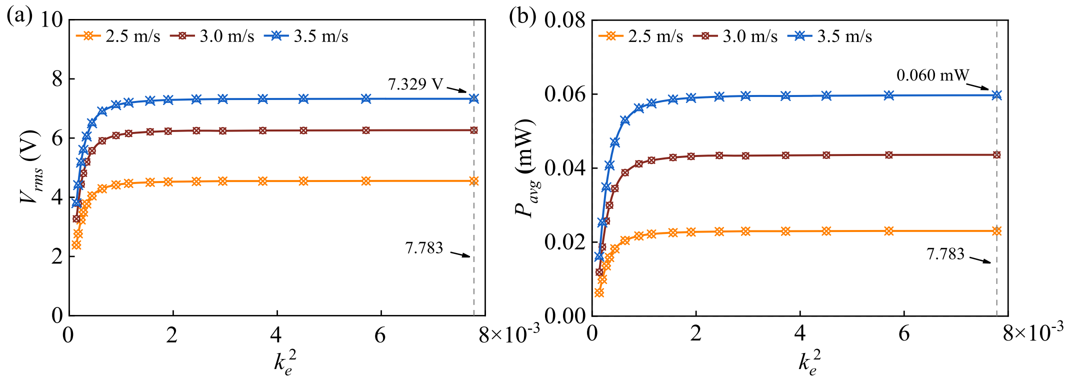

Fig. 20. The variation of (a) the RMS voltage output and (b) the average power with the change of the electromechanical coupling strength under different wind speeds.

${k_e}^2$ is another important factor that affects the energy harvesting performance. It is closely related to the clamped capacitance C_p of piezoelectric transducers. Therefore, we regulate the ${k_e}^2$ by changing C_p. Fig. 20 shows the variations of V_{rms} and P_{avg} with ${k_e}^2$ under different wind speeds. With the increase of ${k_e}^2$, V_{rms} and P_{avg} both first increase rapidly and then tend to saturate. It is unsurprising that V_{rms} and P_{avg} increase with the wind speed. The maximum V_{rms} and P_{avg} obtained at $U = 3.5$ m /s and ${k_e}^2 = 7.783 \times 10^{-3}$ are 7.329 V and 0.06 mW, respectively.

The above studies indicate that the performance of wind energy harvesters can be enhanced by appropriately tuning the load resistance and increasing the electromechanical coupling strength, even if the mechanical structure is already determined. However, arbitrarily increasing ${k_e}^2$ is unwise. Piezoelectric materials with higher coupling coefficients are usually more expensive. As revealed in Fig. 20, the power output of a harvester saturates when the electromechanical coupling strength is sufficiently large. An excessive increase of ${k_e}^2$ will only raise the bare cost but not boost the energy harvesting efficiency.

7. Conclusions

This article has presented several novel bluff bodies etched with metasurface patterns for VIV energy harvesting. Wind tunnel experiments have been conducted to explore the influences of metasurface patterns on the dynamic behaviors and the energy harvesting performance. A lumped parameter model based on the van der pool wake oscillator equation has been developed to predict the energy harvesting performance.

According to the experimental results, the metasurface patterns can be classified into three categories depending on whether they can enhance or suppress VIV. The metasurface in the concave H pattern belongs to the first category that reinforces VIV and is beneficial for wind energy harvesting. Compared to the baseline model, which uses a smooth cylinder bluff body, the maximum RMS output voltage produced by the concave H model is increased by 9.44%. Moreover, the effective working bandwidth (i.e., the lock-in region) of the concave H model is enlarged by 30.77%. The second category includes the concave C, P, and W metasurface patterns. Etching the second category of metasurface patterns on a cylinder bluff body leads to significant suppression of VIV. Therefore, the energy harvesting performance deteriorates, i.e., the maximum RMS voltage output decreases, and the effective working bandwidth narrows down. The last category, including the concave S and T metasurface patterns, has inapplicable influences on the aerodynamics of the bluff body. CFD simulations have been conducted to provide insights into how the metasurface patterns affect the aerodynamics of bluff bodies.

The vorticity contours of three different bluff bodies have been simulated to unveil the vortex-shedding process. It has been demonstrated that different metasurface patterns result in the formation of different vortex streets behind the bluff bodies and produce different aerodynamic forces on the bluff bodies, thus, affecting the performance of energy harvesting.

Finally, based on the theoretical model, parametric studies have been carried out to investigate the effects of several electrical parameters on energy harvesting performance. The results have indicated that achieving impedance matching and having a sufficiently large electromechanical coupling strength are pivotal to maximizing the power output. However, the power saturation phenomenon suggests that arbitrarily increasing the electromechanical coupling strength is unwise and will only lead to an increment in cost.

CRediT authorship contribution statement

Junlei Wang: Conceptualization, Investigation, Formal analysis, Writing – original draft, Funding acquisition. **Ye Zhang:** Writing – original draft, Investigation, Data curation, Software, Visualization. **Ming Liu:** Investigation, Writing – review & editing. **Guobiao Hu:** Conceptualization, Supervision, Formal analysis, Writing – review & editing.

Declaration of Competing Interest

The authors declare that they have no known competing financial interests or personal relationships that could have appeared to influence the work reported in this paper.

Data availability

None.

Acknowledgments

This work was supported by the National Natural Science Foundation of China (Grant No.: 51977196, 52277227), China Postdoctoral Science Foundation (2020T130557), Henan Province Science Foundation for Youths (202300410422), State Key Laboratory of Coastal and Offshore Engineering (LP2216), and Soyotec Technologies Co., Ltd. (Beijing) on XFlow Software.

References

[1] Ellingsen OM, Flamand O, Amandolese X, Coiffet F, Hemon P. Field tests on a full-scale steel chimney subjected to vortex-induced vibrations. Struct Eng Int 2022;32 (1):55–61.
[2] Cheng L, Luan T, Du W, Xu M. Heat transfer enhancement by flow-induced vibration in heat exchangers. Int J Heat Mass Transf 2009;52(3–4):1053–7.
[3] Zafar F, Alam MM. Flow structure around and heat transfer from cylinders modified from square to circular. Phys Fluids 2019;31(8):083604.
[4] Wang JL, Tang LH, Zhao LY, Zhang Z. Efficiency investigation on energy harvesting from airflows in HVAC system based on galloping of isosceles triangle sectioned bluff bodies. Energy 2019;172:1066–78.
[5] Zhu HJ, Yao J. Numerical evaluation of passive control of VIV by small control rods. Appl Ocean Res 2015;51:93–116.
[6] Zhu HJ, Yao J, Ma Y, Zhao HN, Tang YB. Simultaneous CFD evaluation of VIV suppression using smaller control cylinders. J Fluids Struct 2015;57:66–80.
[7] Chen WL, Ji CN, Williams J, Xu D, Yang LH, Cui YT. Vortex-induced vibrations of three tandem cylinders in laminar cross-flow: vibration response and galloping mechanism. J Fluids Struct 2018;78:215–38.
[8] Wang JL, Yurchenko D, Hu GB, Zhao LY, Tang LH, Yang YW. Perspectives in flow-induced vibration energy harvesting. Appl Phys Lett 2021;119(10):100502.
[9] Paidoussis, M.P., Price, S.J., and Langre, E.D., Fluid-structure interactions: Cross-flow-induced instabilities. 2011.
[10] Zhang HR, Sui WT, Yang CQ, Zhang LA, Sun Z, Guo X, et al. An asymmetric magnetic-coupled bending-torsion piezoelectric energy harvester: modeling and experimental investigation. Smart Mater Struct 2022;31:015037.
[11] Zhao LC, Zou HX, Yan G, Liu FR, Tan T, Wei KX, Zhang WM. Magnetic coupling and flextensional amplification mechanisms for high-robustness ambient wind energy harvesting. Energy Convers Manag 2019;201:112166.
[12] Zou HX, Zhang WM, Li WB, Hu KM, Wei KX, Peng ZK, Meng G. A broadband compressive-mode vibration energy harvester enhanced by magnetic force intervention approach. Appl Phys Lett 2017;110(16):163904.
[13] Kan J, Wang J, Wu Y, Chen S, Wang S, Jiang Y, Zhang Z. Energy harvesting from wind by an axially retractable bracket-shaped piezoelectric vibrator excited by magnetic force. Energy 2022;240:122495.
[14] Zhu HJ, Zhao Y, Zhou TM. CFD analysis of energy harvesting from flow induced vibration of a circular cylinder with an attached free-to-rotate pentagram impeller. Appl Energy 2018;212:304–21.
[15] Cao DX, Wang JR, Guo XY. et al. Recent advancement of flow-induced piezoelectric vibration energy harvesting techniques: principles, structures, and nonlinear designs. Appl Math Mech 2022;43(7):959–78.
[16] Zhao LC, Zou HX, Yan G, Liu FR, Tan T, Zhang WM, Peng ZK, Meng G. A water-proof magnetically coupled piezoelectric-electromagnetic hybrid wind energy harvester. Appl Energy 2019;239:735–46.
[17] Kan J, Liao W, Wang J, Wang S, Yan M, Jiang Y, Zhang Z. Enhanced piezoelectric wind-induced vibration energy harvester via the interplay between cylindrical shell and diamond-shaped baffle. Nano Energy 2021;89:106466.
[18] Fang S, Xing J, Chen K, et al. Hybridizing piezoelectric and electromagnetic mechanisms with dynamic bistability for enhancing low-frequency rotational energy harvesting. Applied Physics Letters 2021;119(24):243903.
[19] Cepnik C, Radler O, Rosenbaum S, Strohla T, Wallrabe U. Effective optimization of electromagnetic energy harvesters through direct computation of the electromagnetic coupling. Sens Actuators A Phys 2011;167(2):416–21.

[20] Hou CW, Li CH, Shan XB, Yang CQ, Song RJ, Xie T. A broadband piezo-electromagnetic hybrid energy harvester under combined vortex-induced and base excitations. Mech Syst Signal Process 2022;171:108963.

[21] Zhao LC, Zou HX, Zhao YJ, Wu ZY, Liu FR, Wei KX, Zhang WM. Hybrid energy harvesting for self-powered rotor condition monitoring using maximal utilization strategy in structural space and operation process. Appl Energy 2022;314:118983.

[22] Torres EO, Rincon-Mora GA. Electrostatic energy-harvesting and battery-charging CMOS system prototype. IEEE Trans Circuits Syst Regul Pap 2009;56(9):1938–48.

[23] Wang F, Hansen O. Electrostatic energy harvesting device with out-of-the-plane gap closing scheme. Sens Actuators A Phys 2014;211:131–7.

[24] Zhang YL, Wang TY, Luo AX, Hu YS, Li X, Wang F. Micro electrostatic energy harvester with both broad bandwidth and high normalized power density. Appl Energy 2018;212:362–71.

[25] Zhang CG, Liu YB, Zhang BF, Yang O, Yuan W, He LX, Wei XL, Wang J, Wang ZL. Harvesting wind energy by a triboelectric nanogenerator for an intelligent high-speed train system. ACS Energy Lett 2021;6(4):1490–9.

[26] Zhang LB, Meng B, Xia Y, Deng ZM, Dai HL, Hagedorn P, Peng ZC, Wang L. Galloping triboelectric nanogenerator for energy harvesting under low wind speed. Nano Energy 2020;70:104477.

[27] Hu GB, Zhao CY, Yang YY, Li X, Liang JR. Triboelectric energy harvesting using an origami-inspired structure. Appl Energy 2022;306:118037.

[28] Zou HX, Zhao LC, Wang Q, Gao QH, Yan G, Wei KX, Zhang WM. A self-regulation strategy for triboelectric nanogenerator and self-powered wind-speed sensor. Nano Energy 2022;95:106990.

[29] Lu ZS, Zhang HH, Mao CP, Li CM. Silk fabric-based wearable thermoelectric generator for energy harvesting from the human body. Appl Energy 2016;164:57–63.

[30] Raissi M, Wang ZE, Triantafyllou MS, Karniadakis GE. Deep learning of vortex-induced vibrations. J Fluid Mech 2018;861:119–37.

[31] Mehmood A, Abdelkefi A, Hajj MR, Nayfeh AH, Akhtar I, Nuhait AO. Piezoelectric energy harvesting from vortex-induced vibrations of circular cylinder. J Sound Vib 2013;332(19):4656–67.

[32] Lai ZH, Wang SB, Zhu LK, Zhang GQ, Wang JL, Yang K, Yurchenko D. A hybrid piezo-dielectric wind energy harvester for high-performance vortex-induced vibration energy harvesting. Mech Syst Signal Process 2021;150:107212.

[33] Wang S, Liao W, Zhang Z, Liao Y, Yan M, Kan J. Development of a novel non-contact piezoelectric wind energy harvester excited by vortex-induced vibration. Energy Convers Manag 2021;235:113980.

[34] Wang JL, Geng LF, Ding L, Zhu HJ, Yurchenko D. The state-of-the-art review on energy harvesting from flow-induced vibrations. Appl Energy 2020;267:114902.

[35] Yang K, Wang JL, Yurchenko D. A double-beam piezo-magneto-elastic wind energy harvester for improving the galloping-based energy harvesting. Appl Phys Lett 2019;115(19):193901.

[36] Chen ZS, Tse KT, Kwok KCS, Kareem A, Kim B. Measurement of unsteady aerodynamic force on a galloping prism in a turbulent flow: a hybrid aeroelastic-pressure balance. J Fluids Struct 2021;102:103232.

[37] Hu GB, Wang JL, Tang LH. A comb-like beam based piezoelectric system for galloping energy harvesting. Mech Syst Signal Process 2021;150:107301.

[38] Bryant M, Garcia E. Modeling and testing of a novel aeroelastic flutter energy harvester. J Vib Acoust Trans ASME 2011;133(1):011012.

[39] Orrego S, Shoele K, Ruas A, Doran K, Caggiano B, Mittal R, Kang SH. Harvesting ambient wind energy with an inverted piezoelectric flag. Appl Energy 2017;194:212–22.

[40] Li ZY, Zhou SX, Li X. A piezoelectric-electromagnetic hybrid flutter-based wind energy harvester: Modeling and nonlinear analysis. Int J Nonlin Mech 2022;144:104051.

[41] Xu ZW, Dai GL, Zhang LM, Chen YF, Flay RGJ, Rao HM. Effect of non-Gaussian turbulence on extreme buffeting response of a high-speed railway sea-crossing bridge. J Wind Eng Ind Aerodyn 2022;224:104981.

[42] Su Y, Di J, Zuo TZ, Li SP, Qin FJ. Buffeting response evaluation of slender linear structures considering the influence of the aspect ratio on the scale effect. J Sound Vib 2022;530:116969.

[43] Ma XQ, Li ZY, Zhang H, Zhou SX. Dynamic modeling and experiment of a tristable vortex-induced vibration energy harvester. Mech Syst Signal Process 2023;187:109924.

[44] Bishop RED, Hassan AY. The lift and drag forces on a circular cylinder oscillating in a flowing fluid. Proc R Soc Lond Ser A Math Phys Sci 1964;277(1368):25–51.

[45] Dai HL, Abdelkefi A, Wang L. Theoretical modeling and nonlinear analysis of piezoelectric energy harvesting from vortex-induced vibrations. J Intell Mater Syst Struct 2014;25(14):1861–74.

[46] Wang JL, Tang LH, Zhao LY, Hu GB, Song RJ, Xu K. Equivalent circuit representation of a vortex-induced vibration-based energy harvester using a semi-empirical lumped parameter approach. Int J Energy Res 2020;44(6):4516–28.

[47] Gu MF, Song BW, Zhang BS, Mao ZY, Tian WL. The effects of submergence depth on Vortex-Induced Vibration (VIV) and energy harvesting of a circular cylinder. Renew Energy 2020;151:931–45.

[48] Zhang HI, Fan BC, Chen ZH, Li HZ. Numerical study of the suppression mechanism of vortex-induced vibration by symmetric Lorentz forces. J Fluids Struct 2014;48:62–80.

[49] Ding L, Zhang L, Wu CM, Mao XR, Jiang DY. Flow induced motion and energy harvesting of bluff bodies with different cross sections. Energy Convers Manag 2015;91:416–26.

[50] Zhu HJ, Li GM, Wang JL. Flow-induced vibration of a circular cylinder with splitter plates placed upstream and downstream individually and simultaneously. Appl Ocean Res 2020;97:102084.

[51] Ding L, Yang L, Yang ZM, Zhang L, Wu CM, Yan BW. Performance improvement of aeroelastic energy harvesters with two symmetrical fin-shaped rods. J Wind Eng Ind Aerodyn 2020;196:104051.

[52] Zhou SX, Wang JL. Dual serial vortex-induced energy harvesting system for enhanced energy harvesting. AIP Adv 2018;8(7):075221.

[53] Wang JL, Zhou SX, Zhang ZE, Yurchenko D. High-performance piezoelectric wind energy harvester with Y-shaped attachments. Energy Convers Manag 2019;181:645–52.

[54] Azadeh-Ranjbar V, Elvin N, Andreopoulos Y. Vortex-induced vibration of finite-length circular cylinders with spanwise free-ends: broadening the lock-in envelope. Phys Fluids 2018;30(10):105104.

[55] Gao Y, Zhang ZZ, Zou L, Liu LM, Yang B. Effect of surface roughness and initial gap on the vortex-induced vibrations of a freely vibrating cylinder in the vicinity of a plane wall. Mar struct 2020;69:102663.

[56] Huang S. VIV suppression of a two-degree-of-freedom circular cylinder and drag reduction of a fixed circular cylinder by the use of helical grooves. J Fluids Struct 2011;27(7):1124–33.

[57] Zhu HJ, Liu WL. Flow control and vibration response of a circular cylinder attached with a wavy plate. Ocean Eng 2020;212:107537.

[58] Jin ZL, Li GL, Wang JL, Zhang ZI. Design, modeling, and experiments of the vortex-induced vibration piezoelectric energy harvester with bionic attachments. Complexity 2019;2019:1670284.

[59] Wang JL, Sun SK, Tang LH, Hu GB, Liang JR. On the use of metasurface for Vortex-Induced vibration suppression or energy harvesting. Energy Convers Manag 2021;235:113991.

[60] Cummer SA, Christensen J, Alu A. Controlling sound with acoustic metamaterials. Nat Rev Mater 2016;1(3):16001.

[61] Xie BY, Tang K, Cheng H, Liu ZY, Chen SQ, Tian JG. Coding acoustic metasurfaces. Adv Mater 2017;29(6):1603507.

[62] Zhang L, Chen MZ, Tang WK, Dai JY, Miao L, Zhou XY, Jin S, Cheng Q, Cui TJ. A wireless communication scheme based on space- and frequency-division multiplexing using digital metasurfaces. Nat Electron 2021;4(3):218–27.

[63] Falade OP, Jilani SF, Ahmed AY, Wildsmith T, Reip P, Rajab KZ, Alomainy A. Design and characterisation of a screen-printed millimetre-wave flexible metasurface using copper ink for communication applications. Flex Print Electron 2018;3(4):045005.

[64] Wu C, Arju N, Kelp G, Fan JA, Dominguez J, Gonzales E, Tutuc E, Brener I, Shvets G. Spectrally selective chiral silicon metasurfaces based on infrared Fano resonances. Nat Commun 2014;5:3892.

[65] Ma GC, Yang M, Xiao SW, Yang ZY, Sheng P. Acoustic metasurface with hybrid resonances. Nat Mater 2014;13(9):873–8.

[66] Wu JB, Shen Z, Ge SJ, Chen BW, Shen ZX, Wang TF, Zhang CH, Hu W, Fan KB, Padilla W, Lu YQ, Jin BB, Chen J, Wu PH. Liquid crystal programmable metasurface for terahertz beam steering. Appl Phys Lett 2020;116(13):131104.

[67] Shalaginov MY, Campbell SD, An SS, Zhang YF, Rios C, Whiting EB, Wu YH, Kang L, Zheng BW, Fowler C, Zhang HL, Werner DH, Hu JJ, Gu T. Design for quality: reconfigurable flat optics based on active metasurfaces. Nanophotonics 2020;9(11):3505–34.

[68] Erturk A, Inman DJ. Issues in mathematical modeling of piezoelectric energy harvesters. Smart Mater Struct 2008;17(6):065016.

[69] Facchinetti ML, de Langre E, Biolley F. Coupling of structure and wake oscillators in vortex-induced vibrations. J Fluids Struct 2004;19(2):123–40.

[70] Blevins, R.D. (1977). *Flow-induced vibration.* New York.

[71] Krenk S, Nielsen SR. Energy balanced double oscillator model for vortex-induced vibrations. J Eng Mech 1999;125(3):263–71.

[72] Shang GQ, Wang HB, Sun CH. On mathematical modeling of piezoelectric energy harvesters. Adv Mater Res 2014;953(954):655–8.

[73] Aidun CK, Clausen JR. Lattice-Boltzmann method for complex flows. Annu Rev Fluid Mech 2010;42(1):439–72.

[74] Suga K, Kuwata Y, Takashima K, Chikasue R. A D3Q27 multiple-relaxation-time lattice Boltzmann method for turbulent flows. Comput Math Appl 2015;69(6):518–29.

[75] Bhatnagar PL, Gross EP, Krook M. A model for collision processes in gases. I. Small amplitude processes in charged and neutral one-component systems. Phys Rev 1954;94(3):511–25.

[76] Murakami S, Iizuka S, Ooka R. CFD analysis of turbulent flow past square cylinder using dynamic LES. J Fluids Struct 1999;13(7–8):1097–112.

[77] Han SL, Yu RX, Li ZY, Wang YY. Effect of turbulence model on simulation of vehicle aerodynamic characteristics based on XFlow. Appl Mech Mater 2013;457(458):1571–4.

[78] Yu HD, Girimaji SS. Near-field turbulent simulations of rectangular jets using lattice Boltzmann method. Phys Fluids 2005;17(12):125106.